New response in electrochemical impedance spectroscopy due to the presence of molybdenum on AB$_5$-type alloys

CrossMark

Verónica Díaz [a,*], Rita Humana [b,c], Erika Teliz [d], Fabricio Ruiz [e,f],
Elida Castro [b,†], Ricardo Faccio [g], Fernando Zinola [d]

[a] Universidad de la República, Facultad de Ingeniería, Instituto de Ingeniería Química, Núcleo Interdisciplinario Ingeniería Electroquímica, J.Herrera y Reissig 565, CP 11300, Montevideo, Uruguay
[b] Universidad Nacional de La Plata, Instituto de Investigaciones Fisicoquímicas Teóricas y Aplicadas (INIFTA), Facultad de Ciencias Exactas, CCT La Plata-CONICET, CC 16, Suc. 4, (1900), La Plata, Argentina
[c] Universidad Nacional de Catamarca, Facultad de Ciencias Exactas y Naturales, Av. Belgrano Nᵒ 300 (4700), Catamarca, Argentina
[d] Universidad de la República, Facultad de Ciencias, Laboratorio de Electroquímica Fundamental, Núcleo Interdisciplinario Ingeniería Electroquímica, Igua 4225, CP 11400, Montevideo, Uruguay
[e] Consejo Nacional de Investigaciones Científicas y Técnicas, CONICET, Av. Rivadavia 1917, C1033AAJ, Ciudad de Buenos Aires, Argentina
[f] Centro Atómico Bariloche, Comisión Nacional de Energía Atómica (CAB-CNEA), Av. Bustillo 9500, CP 8400, S.C. de Bariloche, RN, Argentina
[g] Universidad de la República, Crystallography, Solid State and Materials Laboratory (Cryssmat-Lab), DETEMA, Centro NanoMat, Polo Tecnológico de Pando, Espacio Interdisciplinario, Facultad de Química, Montevideo, Uruguay

ARTICLE INFO

ABSTRACT

During the present investigation, it was observed that the inclusion of molybdenum in LaNi$_{3.6}$Co$_{0.7}$Mn$_{(0.4-x)}$Al$_{0.3}$Mo$_x$ AB5-type alloys produced new responses in the electrochemical impedance spectroscopy (EIS) when they are used as an anode active material for Ni-MH batteries. The aim of this work is to study, using electrochemical impedance spectroscopy, the influence of molybdenum, on the performance of the electrode. EIS spectra were adjusted in terms of a physicochemical model of the dynamic response of the system. X ray diffraction and hydrogen diffusion coefficient calculated from discharges curves supported EIS model outcomes.

The replacement of manganese by molybdenum, in a 2% w/w concentration level (AB$_5$M1), has a positive effect for applications as energy storage material. In this sense, this alloy exhibits the lowest value of charge transfer resistance obtained from the analysis of impedance spectra. Moreover, changes in the (i_0. a_a) parameter, that is, the exchange current density and active area, respectively display a maximum value. The larger grade of

fracture observed in AB$_5$M1 can be due to the higher material's fragility as a consequence of molybdenum incorporation. XRD analysis on the three alloys confirms this hypothesis as shown in the paper.

Introduction

Nickel/metal hydride (Ni/MH) rechargeable batteries are widely used in consumer portable devices and hybrid electric vehicles [1—3]. Active materials of Ni/MH battery are composed by a metal hydride alloy (as anode) and NiOOH (as cathode).

Multi-component alloying is one of the most effective techniques to tailor electrochemical performances of metal hydride alloys [4,5]. The alloy composition is a critical factor that influences the hydrogen sorption kinetics and electrochemical behavior of the Ni/MH battery anode [6].

Molybdenum (Mo) is an interesting element to modify a metal hydride alloy [7—12] due to its interesting characteristic as a hydrogen-absorption material. In a previous work we found that the replacement of manganese by molybdenum, in the intermediate concentration tested (Mo 2% w/w) has a positive effect [13] in many physical and chemical properties. The influence of the Mo on the electrode performance was studied by potentiodynamic and galvanostatic techniques.

The alloy corresponding to this concentration (AB5M1) presents the closest potential to system equilibrium potential and therefore the lowest overpotentials. We have found that this alloy also has a great electrochemical behavior for rate discharges in the range of 0.1—1C. These facts could be associated with a higher exchange current density (i_o), a higher diffusion coefficient (D_H) and/or a smaller alloy particle radius (r_a) when comparing to the others compounds. In order to clarify the processes which are really being influenced by the new incorporation of Mo, in the present work electrochemical impedance spectra (EIS) were taken and adjusted in terms of a physicochemical model of the dynamic response of the system. Evidences of X ray diffraction and high rate discharge ability supported these outcomes.

Experimental

Synthesis of alloys

The studied alloys were prepared by arc melting adequate proportions of the composition elements (purity better than 99.9%) inside a copper-cooled hearth under high purity argon (99.998%). To improve the purity of the melting atmosphere, a sacrifice button of Zirconium (Zr) was previously melted. The resulting alloy buttons were turned over and remelted at least twice to ensure homogeneity.

Three alloys were synthesized replacing manganese by molybdenum, obtaining the following alloys, presented in Table 1.

Structural and microstructural characterization of MH electrodes

The electrodes were subjected to X-ray diffraction characterization. X-ray powder diffraction data were collected using a Rigaku ULTIMA IV, 285 mm radius, powder diffractometer operating in Bragg Brentano geometry. To collect data over the 10—110° 2θ range in steps of 0.02° using a scintillation detector, a CuKα radiation (λ = 1.5418 Å) monochromatized with a diffracted beam bent germanium crystal was used. In order to prevent beam spillage outside the 2 cm long sample (along the beam-path) at low angles, fixed slits of 1/3° were used for data collection. Peak positions were extracted from the data using the software POWDERX [14]. Unit cell determination and peak indexing were performed with the software DICVOL04 [15]. The space group symmetry of the crystalline samples was determined.

Further analysis consisted in the full pattern profile fitting, using the Rietveld method [16] by means of the EXPGUI-GSAS suite [17,18] that allowed the drawing out of relevant structural parameters and weight fraction for multiphase systems.

The surface alloy microstructures were examined by means of a scanning electron microscope (SEM, JEOL JSM 5900) with a 25 kV secondary electron imaging mode.

Electrochemical characterization

For the electrochemical characterization, the alloy buttons were mechanically crushed and the resulting powders were used in the preparation of the negative electrodes. They were prepared by compacting a mixture of 100 mg of sample powders with equal amounts of teflonized carbon (Vulcan XC-72), inside a cylindrical die to a pressure of 250 MPa at room temperature. The electrode geometrical area was 2 cm^2 and the thickness was around 1 mm. A nickel wire was used as a current collector.

Electrochemical measurements were conducted in an electrochemical cell with the alloy as working (in the form of a metal hydride electrode), a nickel mesh as counter and an alkaline Hg/HgO reference electrode. The electrolyte, a 60 M KOH solution, was prepared from KOH reagent grade and Millipore-MilliQ® plus water.

For the charge—discharge cycle tests, negative electrodes were charged at −100 mA/g for 4 h and, and subsequently discharged at 50 mA/g to a cut-off potential of −0.60 V vs Hg/HgO. EIS measurements were performed once the alloys had reached their maximum capacity after the activation. The

Table 1 – Labels, compositions and mass percentages of molybdenum in the manufactured alloys.			
Label	AB$_5$M0	AB$_5$M1	AB$_5$M2
Chemical composition	LaNi$_{3.6}$Co$_{0.7}$Mn$_{0.4}$Al$_{0.3}$	LaNi$_{3.6}$Co$_{0.7}$Mn$_{0.3}$Al$_{0.3}$Mo$_{0.1}$	LaNi$_{3.6}$Co$_{0.7}$Mn$_{0.15}$Al$_{0.3}$Mo$_{0.25}$
Mo % w/w	0	2	5

electrodes were discharged to a state of charge (SOC) of 70%, and left at open circuit potential (E_{OCP}). EIS spectra were recorded, at E_{OCP}, in the 50 kHz - 1 mHz frequency range, with a 6 mV amplitude, ten points per decade.

All the electrochemical experiments were conducted using a PGZ 301 Voltalab® potentiostat-galvanostat device at room temperature. Rate capability experiments are performed at discharge charges in the range of 0.1C–5C.

Modeling

In the following section a physicochemical model is developed from which the theoretical impedance function of the electrochemical systems, Z_p, is derived. Z_p was fitted to experimental EIS data, in order to identify the structural and kinetic parameters of the analyzed systems. The system is modeled as a porous flooded structure. The corresponding impedance function, Z_p, for highly conductive solids, given by equation (1), has been derived in previous publications [19–22]:

$$Z_p = \frac{L}{A_p \kappa}\left[\frac{1}{\nu \tanh \nu}\right] \quad (1)$$

where:

$$\nu = L\left(\frac{1}{\kappa}\right)^{1/2} Z_i^{-1/2} \quad (2)$$

being A_p the cross section geometric area, L the porous structure thickness, κ the specific conductivity of the electrolyte phase (S cm^{-1}) and Z_i is the impedance of the solid/liquid interface per electrode unit volume (Ω/cm^3). In the derivation of Z_i, a parallel connection between the interfacial double layer impedance (Z_{dl}) and the faradaic process impedance (Z_F), is assumed.

$$Z_i^{-1} = Z_{dl}^{-1} + Z_F^{-1} \quad (3)$$

where

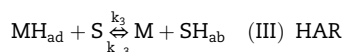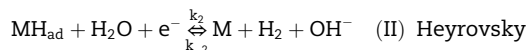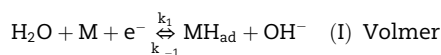$$Z_{dl} = \frac{1}{i\omega C_{dl}a_r} \quad (4)$$

and

$$Z_F = \frac{Z_f}{a_a} \quad (5)$$

being C_{dl} the double layer capacitance per unit area (F/cm^2), a_r the hydrogen/surface area per alloy unit volume (cm^2/cm^3) and $\omega = 2\pi f$ (f, frequency of the perturbing signal). Z_f is the Faradaic impedance per unit active area (Ω/cm^2) and a_a is the active area per alloy unit volume (cm^2/cm^3).

Derivation of Z_f

To derive Z_f, the Volmer-Heyrovsky-HAR (H absorption reaction) mechanism is proposed for the processes of hydrogen

evolution/absorption. These processes are coupled with H diffusion transport within the alloy. The following kinetic mechanism will be used:

$$H_2O + M + e^- \underset{k_{-1}}{\overset{k_1}{\rightleftharpoons}} MH_{ad} + OH^- \quad (I) \text{ Volmer}$$

$$MH_{ad} + H_2O + e^- \underset{k_{-2}}{\overset{k_2}{\rightleftharpoons}} M + H_2 + OH^- \quad (II) \text{ Heyrovsky}$$

$$MH_{ad} + S \underset{k_{-3}}{\overset{k_3}{\rightleftharpoons}} M + SH_{ab} \quad (III) \text{ HAR}$$

The function, Z_f, for this system has been derived in Refs. [23,24] and is written as:

$$Z_f(\omega) = R_{ct} + \frac{AR_{ct}}{F\left(C + \Gamma j\omega + \frac{1-B}{VM(\omega)}\right)} \quad (6)$$

where R_{ct} is the charge transfer resistance, Γ is the maximum surface concentration of the adsorbed reaction intermediate H_{ad} and M is the mass transfer function for spherical geometry. Parameters A, B, C, and V are combinations of kinetic parameters of the reaction steps:

$$A = -F(k_1 + k_{-1} - k_2 - k_{-2}) \quad (7)$$

$$B = 2(F/(RT))(k_2\theta) \quad (8)$$

$$C = 2(k_2 + k_{-2}) \quad (9)$$

$$V = -\left((K_{eq}\theta + (1-\theta))^2\right)\Big/K_{eq} \quad (10)$$

$$K_{eq} = k_3/k_{-3} \quad (11)$$

being K_{eq} the equilibrium constant of the HAR step [25,26]:

$$M(\omega) = \frac{r_a}{C_{max}D_H}\frac{1}{1 - \psi_a \coth(\psi_a)} \quad (12)$$

being:

$$\psi_a = r_a\sqrt{\frac{i\omega}{D_H}} \quad (13)$$

where D_H is the diffusion coefficient of H in the alloy and r_a the average radius of the particles.

Results and discussion

According to XRD difraction patterns, AB5M0 sample is a single phase crystalline alloy, indexed in the corresponding CaCu$_5$-type structure in the P6/mmm space group [27]. In the case of AB$_5$M1 and AB$_5$M2 samples there is coexistence between the CaCu$_5$-type and CaCu$_3$-type crystalline phase. According to Rietveld Refinement, the weight fractions for the Rombohedral phases correspond to 15.9% and 19.3% for

AB$_5$M1 and AB$_5$M2 respectively. The XRD diagrams for AB$_5$M0, AB$_5$M1 and AB$_5$M2 were presented in a previous work [13].

The incorporation of Mo induces the contraction of cell parameters in the crystalline structure of the studied alloys. This phenomenon is accompanied by a coexistence of two crystal structures, with general AB$_5$ and AB$_3$ stoichiometry. The cell parameters contraction, as a result of Mo addition, may be due to changes in the electronic structure of the hybrid compound which escapes from a trivial analysis based on atomic radius of the constituent elements. Theoretical work, based on first principles methods, are carrying out in order to understand the physical origin of the contraction of the unit cell parameters.

According to the full powder profile fitting, it is possible to obtain information related to the physical contribution to the peak profile broadening. In the present work, we selected the well-established Thompson, Cox & Hasting [28] pseudo Voigt model for diffraction line profiles. According to this, the full width at half maximum Γ is contributed from Gaussian and Lorentz functions:

$$\Gamma_G^2 = U \tan^2 \theta + V \tan \theta + W + P/\cos^2 \theta \qquad (14)$$

$$\Gamma_L = \frac{X}{\cos \theta} + Y \tan \theta + Z \qquad (15)$$

U, V, W, X, Y and Z are adjustable parameters and L and G denotes Lorentz and Gauss profiles respectively. The following parameters X, P and U, Y are directly related to size and strain contribution respectively. This is valid if instrumental contributions are taken into account, as our case.

In the case of size broadening, Scherrer [29] equation was considered, and the corresponding crystalline size domain is presented (Table 2). When considering the strain, just a comparison between U and Y parameters are performed, and presented in Table 2. Strain can be obtained independently from Gaussian and Lorentzian terms, presented as S-G and S-L respectively. While some differences emerge from this comparison, the trend is the same for Gaussian and Lorentzian contribution, validating our analysis. These results indicate that AB$_5$M1 sample presents a higher strain when comparing to AB$_5$M0 and AB$_5$M2 samples. In the case of crystalline size domain estimation (CSD), a similar trend is observed, AB$_5$M1 presents the higher CSD with a value of 174 nm, while AB$_5$M0 and AB$_5$M2 present a CSD = 75 nm. In general terms, the XRD results suggest that AB$_5$M1 presents a higher strain, when comparing to AB$_5$M0 and AB$_5$M2 case.

As depicted in the Nyquist diagrams of Fig. 1, the electrodes presented different behaviors depending on the Mo concentration. The apparent charge transfer resistance results in R$_{ct}$AB$_5$M0 > R$_{ct}$AB$_5$M2 > R$_{ct}$AB$_5$M1.

The diagrams show a phase angle close to 45° at high frequencies, characteristic of a porous structure. The capacitive loop in the range of intermediate frequencies is associated with the parallel connection of the electrical double layer, C_{dl}, with the charge transfer resistance, R_{ct}, related to the hydrogen absorption/desorption process on the surface of the alloy particles. In the low frequencies region, a Warburg-type response, associated to the hydrogen diffusion process is observed.

In order to identify the different parameters of the system, a fitting procedure of the experimental impedance data in terms of the proposed model was accomplished.

A fitting programme was developed, based on the Nelder–Meade simplex search algorithm included in the Matlab package. During the fitting procedure the objective function to be minimized was the cost function, J_p, defined as:

$$J_p = \frac{1}{K} \sum_k |e(p, \omega_k)|^2 = \frac{1}{K} \sum_k \left| \frac{Z_e(\omega_k) - Z_p(p, \omega_k)}{Z_e(\omega_k)} \right|^2 \qquad (16)$$

where K is the number of experimental frequencies (ω), and Z_e and Z_p the experimental and theoretical impedance values corresponding to the frequency ω_k. This algorithm returns a parameter vector $[p]$ that is a local minimized of J_p, near the starting vector $[p_0]$, so the whole fitting procedure is highly dependent on the initial values given to the parameters in $[p_0]$. The fitting was considered acceptable when $J_p < 5e{-}3$.

Fig. 1 depicts experimental EIS data of the studied alloys; together with EIS data simulated using the model (see Section 3). From the identified parameters, its dependence with Mo concentration could be determined. A good agreement between measured and calculated data in terms of this model was observed.

According to the fitting procedure of EIS data in terms of equations (1–13), the characteristic parameter values are presented in Table 3.

SEM techniques allow the estimation of the particle size after subjecting the electrodes to several charge/discharge cycles, and thus verify what the physicochemical model predicted from the EIS measurements.

From the micrographics, we can calculate r_a concluding that AB$_5$M1 mean radius is the smallest one [13]. Calculated mean radius values are:

AB$_5$M0/ra = 1.4 × 10^{-3} cm
AB$_5$M1/ra = 5 × 10^{-4} cm
AB$_5$M2/ra = 7.5 × 10^{-4} cm

Fig. 2 shows the dependence of particle radio and active area by exchange current density with molybdenum concentration.

After a brief evaluation and analysis between the behavior of AB$_5$M0, AB$_5$M1 and AB$_5$M2 alloys, we can conclude that the better performance showed by AB$_5$M1 is mainly due to the particles breaking up yielding a larger active area a_a. For this electrode, the changes in the product (i_o a_a) exhibit a

Table 2 – Gaussian and Lorentzian profile fitting parameters, and crystalline size domain and strain obtained from those.

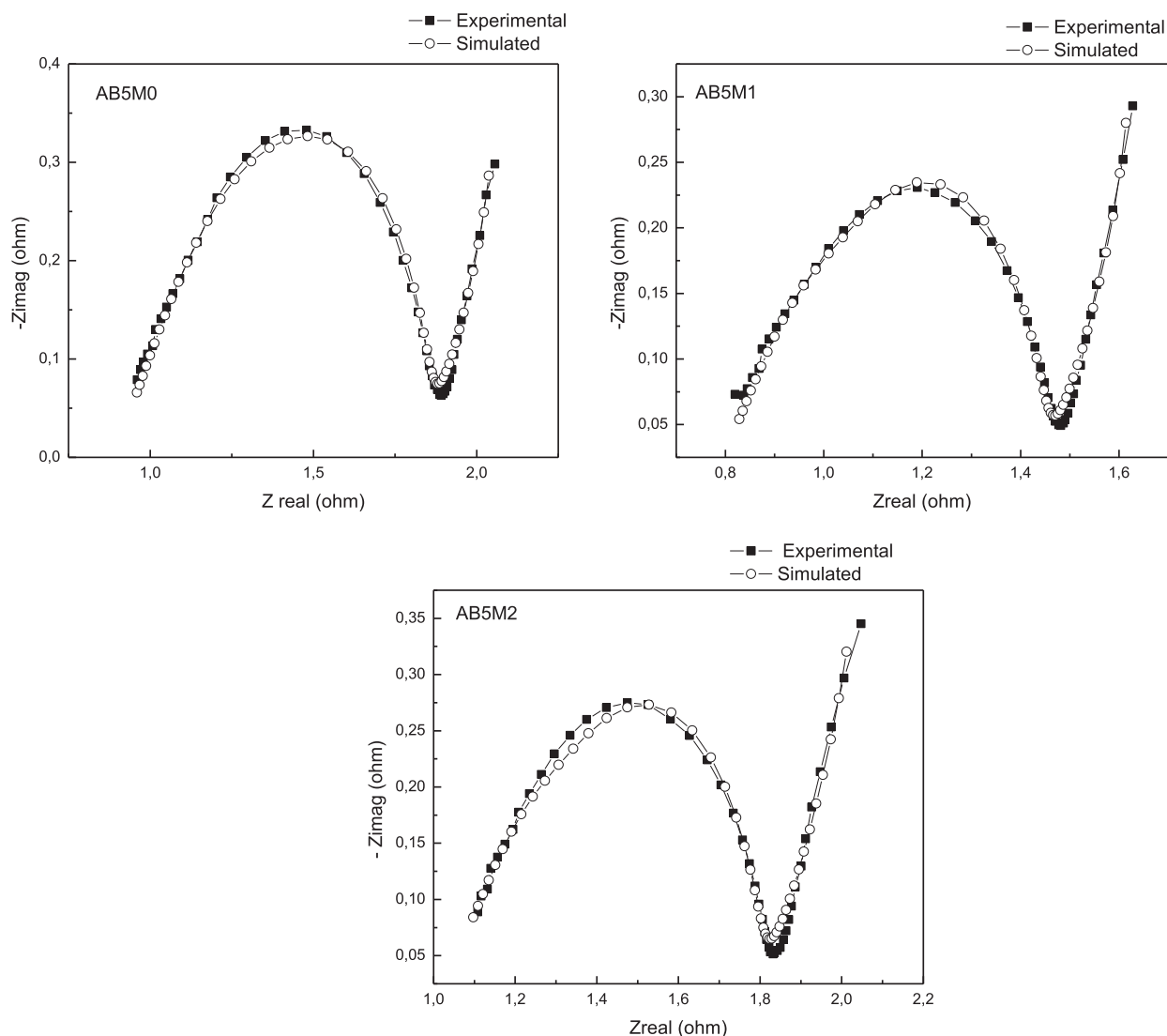|	U	V	W	Lx	Ly	CSD (nm)	S-L (%)	S-G (%)
AB$_5$M0	30.24	−13.35	−17.79	11.03	3.88	75	0.07	0.10
AB$_5$M1	342.69	−56.23	−131.00	6.21	31.41	134	0.55	0.32
AB$_5$M2	69.99	−32.26	−125.14	11.21	4.04	74	0.07	0.15

Fig. 1 – Spectra of experimental and theoretical impedance of the electrodes.

maximum value. Moreover, the minor values of r_a favor the hydrogen mass transport within the alloy, lowering the diffusion overpotential values, *i.e.,* a lower diffusion length. However, it seems that there is almost no difference in the values of i_o and D_H for the three electrodes. The larger fracture of AB_5M1 can be due to the higher material's fragility as a consequence of molybdenum incorporation. XRD analysis on the three alloys confirms this hypothesis.

For **C** discharge rates larger than 4C the alloy AB_5M2 shows a better behavior at HRD experiments than AB_5M0 and AB_5M1. For rate discharges of 0.1–1C the behavior in terms of C/C_{max} is similar in the alloys although AB_5M2 depicts lower capacity.

We include in this study the behavior for HRD with rate discharges of 0.1C–5C (Fig. 3).

Electrochemical determination of the hydrogen diffusion coefficient

In order to analyze the hydrogen transfer rate in the alloy, and compare hydrogen diffusion value with that resulted in EIS phenomenological model, it is assumed a spherical shape to the laboratory-prepared alloy. The hydrogen diffusion balance is given by the second Fick's law:

Table 3 – Parameters derived from the fitting procedure for the three electrodes.

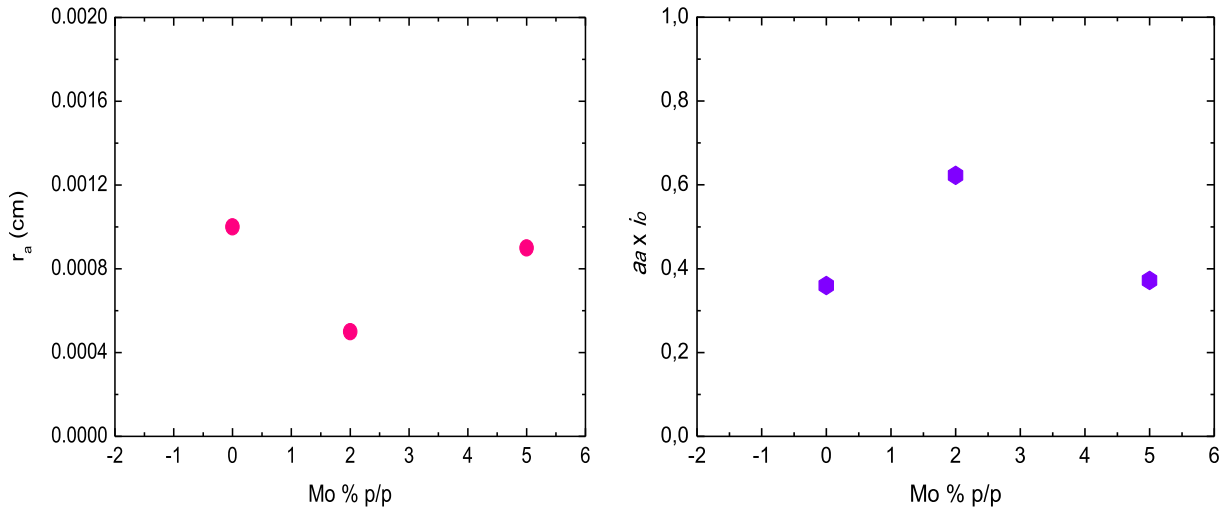| Alloy	D_H (cm^2 s^{-1})	i_o (Acm^{-2})	a_a (cm^2/cm^3)	r_a(cm)	ε	a_r (cm^2/cm^3)
AB_5M0	3.8×10^{-10}	1×10^{-3}	360	1×10^{-3}	0.14	9.5×10^{-4}
AB_5M1	2.7×10^{-10}	0.9×10^{-3}	700	0.5×10^{-3}	0.34	8.6×10^{-4}
AB_5M2	2.7×10^{-10}	1×10^{-3}	351	0.9×10^{-3}	0.25	5.0×10^{-4}

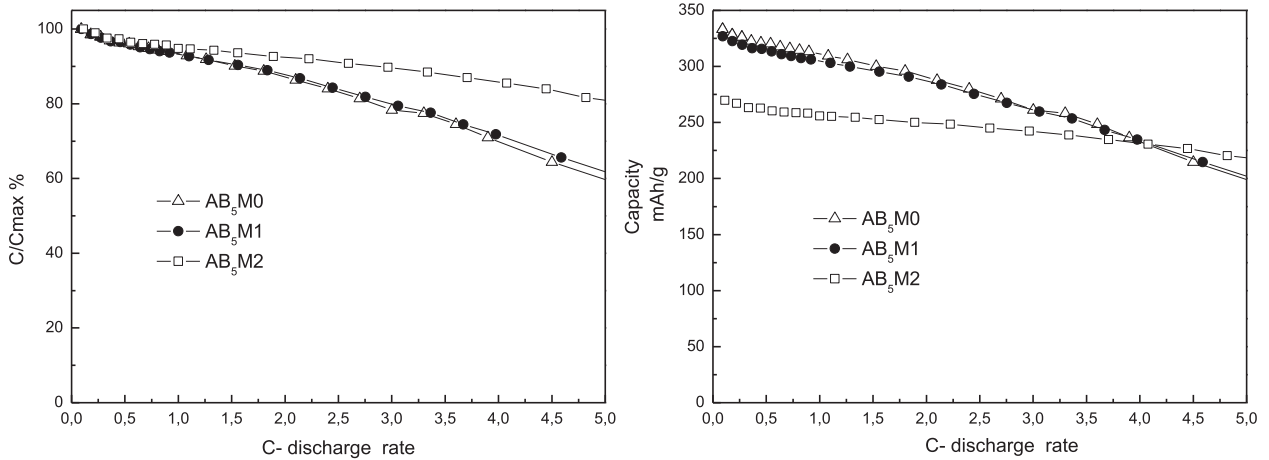**Fig. 2 — Behavior of the parameters r_a and $a_a x\ i_o$ vs [Mo]% w/w.**

Fig. 3 — High rate discharge curves expressed as a percentage of maximum capacity and in mAh/g for AB$_5$M0 (Δ) AB$_5$M1 (●) and AB$_5$M2 (□) alloys.

$$\frac{\partial (RC_H)}{\partial t} = D_H \frac{\partial^2 (RC_H)}{\partial R^2} \quad \frac{\partial (Rc)}{\partial t} = D \frac{\partial^2 (Rc)}{\partial R^2} \tag{17}$$

where C_H is the hydrogen concentration in the alloy, t is time, D_H is an average hydrogen diffusion coefficient, R is the distance from the centre of the sphere to the bulk of the material. Assuming a uniform initial hydrogen concentration in the bulk of the alloy, constant surface concentration, Chen et al. [30] stated that for large values of time, equation (16) reduces to the hydrogen current intensity, $I_H(t)$, time dependence expression:

$$I_H(t) = F \frac{D_H \Delta C_H}{\delta R^2} - \frac{\pi^2 D_H}{R^2} C_H(t) \quad I(t) = F \frac{D \Delta C}{\delta R^2} - \frac{\pi^2 D}{R^2} C(t) \tag{18}$$

Where

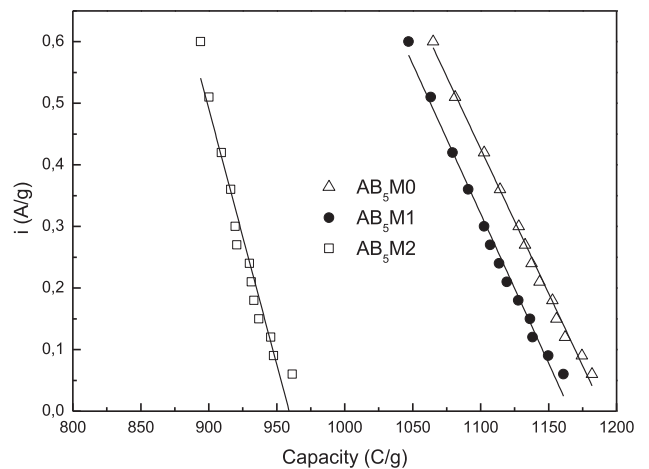$$C_H(t) = \int_0^t I_H(t) dt \quad C(t) = \int_0^t I(t) dt \tag{19}$$

Fig. 4 — . I(t) vs C(t) curve according to equation (17) for AB$_5$M0 (Δ) AB$_5$M1 (●) and AB$_5$M2 (□) alloys. The linear fit is shown with black lines.

Table 4 – Diffusion coefficients resulted from the I(t) vs C(t) plot and EIS fitting data.

	AB$_5$M0	AB$_5$M1	AB$_5$M2
D$_{EIS}$ (cm^2 s^{-1})	3.8×10^{-10}	2.7×10^{-10}	2.7×10^{-10}
D$_{Fig.4}$ (cm^2 s^{-1})	9.3×10^{-10}	1.2×10^{-10}	4.7×10^{-10}

being **F** the Faraday's constant. Knowing the sphere radius, D_H may be evaluated from the slope of the I(t) vs C(t) plot (Fig. 4).

Table 4 depicts D_H values evaluated after taking into account particle radii. It is worth noticing that although these values are quiet different, are in the same order of magnitude to those estimated by the EIS model.

Conclusions

The results show that the concentration of Mo in the AB$_5$ type alloy influences the EIS response. The fitting procedure allowed the identification of typical parameters such as total interfacial area, active area, exchange current density, hydrogen diffusion coefficient, particle radius and porosity. A good agreement between measured and calculated data in terms of this model was observed.

AB$_5$M1 depicts the better performance due to the particles breaking up yielding a larger active area a_a. The transformation of the alloy phase into hydride phase causes the volume expansion of the particle, which produces a large stress at the outside and a compressive stress in the inner part, leading to pulverization of the alloy particles and increasing the active area. The larger fracture of AB$_5$M1 can be due to the higher material's fragility as a consequence of Mo incorporation. XRD results suggest that AB$_5$M1 presents a higher strain, when comparing to AB$_5$M0 and AB$_5$M1 case.

For this electrode, the changes in ($i_0 a_a$) exhibit a maximum value. There is almost no difference on the values of i_0 and D for the three alloy electrodes.

Acknowledgments

R E F E R E N C E S

[1] Peng X, Liu B, Fan Y, Ji L, Zhang B, Zhang Z. Microstructures and electrochemical characteristics of La$_{0.7}$Ce$_{0.3}$Ni$_{4.2}$Mn$_{0.9-x}$Cu$_{0.37}$(V$_{0.81}$Fe$_{0.19}$)$_x$ hydrogen storage alloys. Electrochim Acta 2013;93:207–12.

[2] Xia Y, Yang Y, Shao HX. Differences in the effects of Co and CoO on the performance of Ni(OH)$_2$ electrode in Ni/MH power battery. J Power Sources 2011;196:495–503.

[3] Shangguan E, Wang J, Li J, Dan G, Chang Z, Yuan X, et al. Enhancement of the high-temperature performance of advanced nickel-metal hydride batteries with NaOH electrolyte containing NaBO$_2$. Int J Hydrogen Energy 2013;38(25):10616–24.

[4] Jiang L, Li GX, Xu LQ, Jiang WQ, Lan ZQ, Guo J. Effect of substituting Mn for Ni on the hydrogen storage and electrochemical properties of ReNi$_{2.6-x}$Mn$_x$Co$_{0.9}$ alloys. Int J Hydrogen Energy 2010;35(1):204–9.

[5] Hao JS, Han SM, Li Y, Hu L, Zhang JW. Effects of Fe-substitution for cobalt on electrochemical properties of La-Mg-Ni-based alloys. J Rare Earth 2010;28(2):290–4.

[6] Reilly JJ, Adzic GD, Johnson JR, Vogt T, Mukerjee S, McBreen J. The correlation between composition and electrochemical properties of metal hydride electrodes. J Alloy Compd 1999;293–295:569–82.

[7] Notten PHL, Hokkeling P. Double-phase hydride forming compounds: a new class of highly electrocatalytic materials. J Electrochem Soc 1991;138(7):1877–85.

[8] Senoh H, Hara Y, Inoue H, Iwakura C. Charge efficiency of misch metal-based hydrogen storage alloy electrodes at relatively low temperatures. Electrochim Acta 2001;46(7):967–71.

[9] Young K, Ouchi T, Huang B, Reichman B, Fetcenko MA. Studies of copper as a modifier in C14-predominant AB$_2$ metal hydride alloys. J Power Sources 2012;204:205–12.

[10] Iwakura C, Senoh H, Morimoto K, Hara Y, Inoue H. Influence of temperature on discharge process of misch metal-based hydrogen storage alloy electrodes. Electrochemistry 2002;70(1):2–7.

[11] Yeh MT, Beibutian VM, Hsu SE. Effect of Mo additive on hydrogen absorption of rare-earth based hydrogen storage alloy. J Alloys Compd 1999;293–295:721–3.

[12] Ye H, Zhang H. Development of hydrogen-storage alloys for high-power nickel-metal hydride batteries. Adv Eng Mater 2001;3(7):481.

[13] Díaz V, Teliz E, Ruiz F, Martínez PS, Faccio R, Zinola F. Molybdenum effect on the kinetic behavior of a metal hydride electrode. Int J Hydrogen Energy 2013;38(29):12811–6.

[14] Dong C. PowderX: Windows-95-based program for powder X-ray diffraction data processing. J Appl Cryst 1999;32(4):838.

[15] Boultif A, Louer D. Powder pattern indexing with the dichotomy method. J Appl Cryst 2004;37(5):724–31.

[16] Rietveld HM. A profile refinement method for nuclear and magnetic structures. J Appl Cryst 1969;2(2):65–71.

[17] Larson AC, Von Dreele RB. General structure analysis system (GSAS), Los Alamos National laboratory report LAUR. 2000. p. 86–748.

[18] Toby BH. EXPGUI, a graphical user interface for GSAS. J Appl Crystallogr 2001;34:210–3.

[19] Visintin A, Castro E, Real S, Triaca W, Wang C, Soriaga M. Electrochemical activation and electrocatalytic enhancement of a hydride-forming metal alloy modified with palladium, platinum and nickel. Electrochim Acta 2006;51:3658–67.

[20] Castro E, Real S, Bonesi A, Visintin A, Triaca W. Electrochemical impedance characterization of porous metal hydride electrodes. Electrochim Acta 2004;49:3879–90.

[21] Meyers JP, Doyle M, Darling RM, Newman J. The impedance response of a porous electrode composed of intercalation particles. J Electrochem Soc 2000;147:2930–40.

[22] de Levie R, Delahay P, editors. Advances in electrochemistry and electrochemical engineering, vol. VI. New York: Interscience; 1976. p. 329.

[23] Ruiz FC, Castro EB, Peretti HA, Visintin A. Study of the different Zr_xNi_y phases of Zr-based AB_2 materials. Int J Hydrogen Energy 2010;35:9879–87.

[24] Lundqvist A, Lindbergh G. Kinetic study of a porous metal hydride electrode. Electrochim Acta 1999;44:2523–42.

[25] Castro BE, Milocco RH. Identifiability of sorption and diffusion processes using EIS: application to the hydrogen reaction. J Electroanal Chem 2005;579:113–23.

[26] Jacobsen T, West K. Diffusion impedance in planar, cylindrical and spherical symmetry. Electrochim Acta 1995;40:255–62.

[27] Srivastavaa S, Upadhyay RK. Investigations of AB_5-type negative electrode for nickel-metal hydride cell with regard to electrochemical and microstructural characteristics. J Power Sources 2010;195(9):2996–3001.

[28] Thompson P, Cox DE, Hastings JB. Rietveld refinement of Debye-Scherrer synchrotron X-ray data from Al_2O_3. J Appl Cryst 1987;20:79–83.

[29] Patterson A. The Scherrer Formula for X-ray particle size determination. Phys Rev 1939;56(10):978–82.

[30] Chen J, Dou SX, Bradhurst DH, Liu HK. Studies on the diffusion coefficient of hydrogen through metal hydride electrodes. Int J Hydrogen Energy 1998;23(3):177–82.

Glossary

a_a: active area per electrode unit volume
a_r: interfacial area per unit volume

A_p: electrode geometric area
i_o: exchange current density
C_{dl}: double layer capacitance
C_{max}: maximum H concentration in the alloy
D_H: hydrogen diffusion coefficient in the active material
F: Faraday constant
f: frequency
H: hydrogen
K_2: kinetic constant of the Heyrovsky reaction
L: electrode thickness
M: electrode mass
MH: metal hydride
r_a: average radius of alloy particles
R_t: charge transfer resistance
R: gas constant
T: temperature
V_e: electrode volume
Z_{dl}: double layer capacitance impedance
Z_F: Faradaic reaction impedance
Z_f: Faradaic impedance per unit active area
Z_i: interfacial impedance per unit volume
Z_p: porous impedance function

Greek letters

K: effective electrolyte conductivity
Ω: angular frequency
Γ: maximum surface concentration of H_{ad}